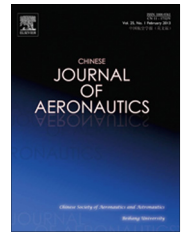




Chinese Society of Aeronautics and Astronautics
& Beihang University

Chinese Journal of Aeronautics

cja@buaa.edu.cn
www.sciencedirect.com



Optimization of endwall contouring in axial compressor S-shaped ducts



Jin Donghai ^{a,*}, Liu Xiwu ^a, Zhao Weiguang ^b, Gui Xingmin ^a

^a School of Energy and Power Engineering, Beihang University, Beijing 100191, China

^b AVIC Aviation Powerplant Research Institute, Hunan 412000, China

Received 21 October 2014; revised 30 March 2015; accepted 11 May 2015
Available online 20 June 2015

KEYWORDS

Adaptive genetic algorithm (AGA);
Artificial neural network (ANN);
Corner separation;
Design of experiments (DOE);
Endwall contouring;
Optimization;
Response surface methodology (RSM);
S-shaped duct

Abstract This paper presents a numerical investigation of the potential aerodynamic benefits of using endwall contouring in a fairly aggressive duct with six struts based on the platform for end-wall design optimization. The platform is constructed by integrating adaptive genetic algorithm (AGA), design of experiments (DOE), response surface methodology (RSM) based on the artificial neural network (ANN), and a 3D Navier–Stokes solver. The visual analysis method based on DOE is used to define the design space and analyze the impact of the design parameters on the target function (response). Optimization of the axisymmetric and the non-axisymmetric endwall contouring in an S-shaped duct is performed and evaluated to minimize the total pressure loss. The optimal ducts are found to reduce the hub corner separation and suppress the migration of the low momentum fluid. The non-axisymmetric endwall contouring is shown to remove the separation completely and reduce the net duct loss by 32.7%.

© 2015 The Authors. Production and hosting by Elsevier Ltd. on behalf of CSAA & BUAA. This is an open access article under the CC BY-NC-ND license (<http://creativecommons.org/licenses/by-nc-nd/4.0/>).

1. Introduction

An S-shaped duct is used to connect the low pressure and high pressure compressors of aircraft gas turbine engines. Within the duct, flow separation should be avoided to minimize the total pressure loss. In addition, a uniform flow field at the duct exit should also be achieved. However, the demands of modern

turbo-fan engines for higher efficiency and lower noise level lead to high by-pass ratio, and result in the engines with large fans and small high pressure compressors, and then bring about a significant radial difference between the low pressure and the high pressure systems. The higher the by-pass ratio is, the more the aggressive S-shaped ducts are needed. This tendency makes duct design increasingly difficult and important. First, transition ducts play a significant role in determining the overall length and weight of the engine. The advantages are obvious if the duct length could be shorter without other penalties. Second, the increase of the thickness of the non-turning struts in the duct would allow improved service access to the core of the engine.

Several researchers have investigated the flows in S-shaped ducts. Bailey et al.¹ investigated the aerodynamic performance of a compressor S-shaped duct with a single strut (the

* Corresponding author. Tel.: +86 10 82339391.

E-mail addresses: jdh@buaa.edu.cn (D. Jin), liuxiwu@buaa.edu.cn (X. Liu).

Peer review under responsibility of Editorial Committee of CJA.



Production and hosting by Elsevier

thickness-chord ratio is 0.12). The blockage of strut was found to have a significant effect on the pressure field of the duct, which has a direct influence on the turbulent flow field. Dueñas et al.² experimentally investigated the effect of reducing the duct length and keeping unchanged the duct inlet height h_{in} and inlet to exit radius change ΔR . It was found that reducing the length of the datum duct without a strut to 74% caused a small increase in loss; however, reducing the length to 64% caused a much greater loss. Walker et al.³ integrated outlet guide vane (OGV) design for an aggressive S-shaped compressor duct and introduced the effects of compressor generated inlet conditions which shown that system length could be reduced by 21% although the overall system loss nominally remained unchanged.

Studies have shown that the limit of the design space of annular S-shaped duct is set by duct corner separation. Reducing the length or increasing the change in radius or the thickness-chord ratio has a similar effect on the duct performance. The streamlines with the maximum curvature, in other words, the flows with the fastest deceleration, emerge in the hub-strut corner, where flow separation may occur. The separation results in a sharp rise of loss coefficient in the duct, and will create a large-scale blockage in the downstream compressor.

In order to reduce the large extent hub-strut corner separation and avoid higher loss coefficient in ducts, the technology of endwall contouring is used in this paper. Endwall profiling has been widely investigated in other turbomachinery components. The successful profiled endwall design begins with Rose⁴, who demonstrated the fundamentals of controlling the endwall static pressure field by means of endwall contouring. That is, convex wall curvature locally accelerates the flow and thus reduces the static pressure, while concave curvature causes diffusion, raising the static pressure. This phenomenon was confirmed in the experiments by Hartland et al.⁵ in the Durham linear cascade. Harvey et al.⁶, Torre et al.⁷, and Sonoda et al.⁸ all had achieved improvements in turbine aerodynamic performance by using endwall contouring through measurement or prediction. The researches of Mahmood⁹ and Gustafson¹⁰ et al. showed that turbine passage endwall heat transfer rates can also be reduced by using endwall profiling. For compressor rotors, Hoeger et al.¹¹ discovered a positive effect of endwall contouring in terms of influencing the shock position. For compressor stator application, Harvey¹² discussed several non-axisymmetric endwall configurations in a linear cascade, and showed that non-axisymmetric endwall, though not optimum, has effects on the crossflow, and the corner stall can be suppressed. Later on, Harvey and Offord¹³ investigated the non-axisymmetric endwall in multi-stage high pressure compressor through computational fluid dynamics (CFD) study, and found that the corner stall can be suppressed either by endwall contouring or 3D-blading. In regard to turbine duct application, Wallin and Eriksson¹⁴ presented studies on CFD-based non-axisymmetric hub endwall shape optimization for an intermediate turbine duct, and showed benefits for duct performance as well as weight reduction. However, the authors found that there were few studies on the use of endwall contouring in compressor ducts. Wallin and Eriksson¹⁵ presented studies on optimization of a 2D axisymmetric turbine duct and a 3D axisymmetric compressor duct by using response surface methodology (RSM). It was found that axisymmetric endwall optimization can reduce duct losses

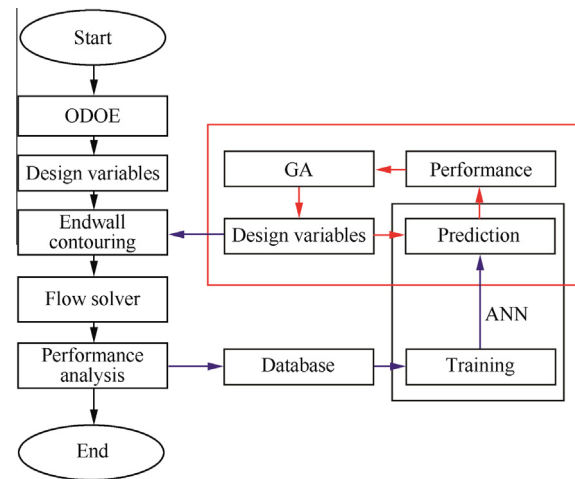


Fig. 1 Flowchart for the algorithm of the endwall design optimization system.

significantly. Naylor et al.¹⁶ used endwall contouring in duct, and showed that the non-axisymmetric endwall completely removed strut-hub corner separation. However, the duct investigated was two-dimensional.

In this paper, the focus lies on intermediate S-shaped duct endwall profiling and its influence on the flow field in the 3D annular duct. A numerical optimization coupling with adaptive genetic algorithm (AGA) and RSM is undertaken to design the axisymmetric and non-axisymmetric endwall profiling. Finally, the performance of the optimal endwall profiling is compared with the datum S-shaped duct.

2. Endwall design optimization platform

The use of design optimization in turbomachinery is possible today thanks to the CFD analysis. Fig. 1 shows the flowchart for the algorithm of the endwall design optimization system. One of its advantages is the use of a response surface model based on an artificial neural network (ANN) as an approximate substitute for the goal-function. The tremendous computational cost of evaluating the endwall performance by 3D CFD can thus be reduced.

The optimization system consists of three steps. First is the training of ANN based on the database provided by the orthogonal design of experiment (ODOE). The second step is the prediction of the optimal aerodynamic performance of endwall contouring by the combination of AGA and ANN, as shown in Fig. 1 with red arrows. Finally, a comparison of the performance obtained by CFD with that of the one predicted by the ANN is executed. If the design requirements are not achieved, the evaluations computed by CFD are added to the database, and the loop is repeated until an optimal geometry is obtained. A more detailed description of the optimization method can refer to Jin^{17–19} and Ning and Liu.²⁰ The following subsections summarize some components and their applications.

2.1. Endwall parameterization

Fig. 2 presents the parameterization of axisymmetric endwall contouring. The parameterization is performed adopting a B-

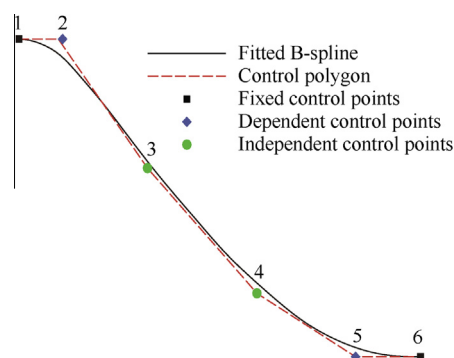


Fig. 2 Axisymmetric endwall parameterization.

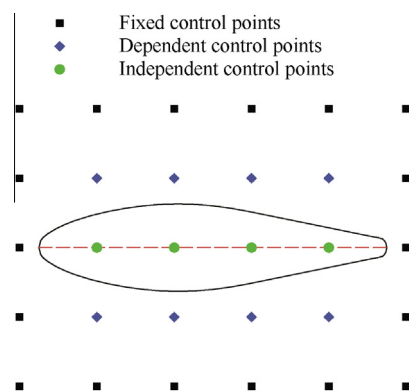


Fig. 3 Non-axisymmetric endwall parameterization.

spline curve controlled by six points in the axial direction. The axial direction represents the direction of engine axis. In order to maintain the continuity of endwall contouring with the low pressure and high pressure systems in the axial direction, points 1 and 6 are fixed. The second point from each end of the curve is used to maintain an approximate continuity of the first derivative of the B-spline curve. For instance, the position of the dependent control point 2, as shown in Fig. 2, is set in the way that the slope of the line passing through points 1 and 2 is close to the slope of the starting of the contour. The independent control points 3 and 4 can move freely. Therefore, there are four design variables for each endwall.

The parameterization of non-axisymmetric endwall is demonstrated in Fig. 3. It is possible to place a set of control points at any axial location. Meanwhile, at a given axial location, any number of control points can be placed, and are then used to generate a B-spline curve in the circumferential direction. The contoured surface is generated by passing through these B-spline curves. At the boundary of the contoured endwall, the black square control points are fixed to maintain the surface continuity as shown in Fig. 3. At a given axial location, the positions of the dependent control points (diamond points) are changed in such a way that the slope of surface continuity is maintained in the circumferential direction as shown in Fig. 4. The position of the independent control points can be changed in the direction perpendicular to the page independently. Once the B-spline curves are generated at each axial location, a surface is lofted through all the curves, which is the required contoured surface for specified parameter values.

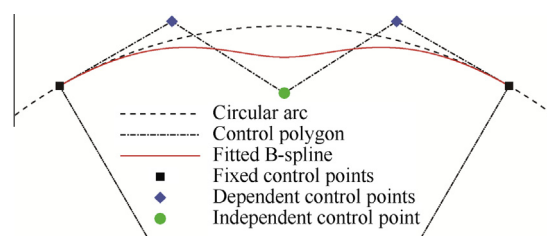


Fig. 4 B-spline curve fitting at a given axial location.

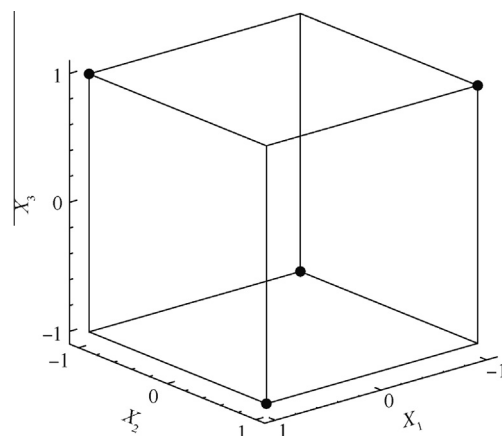


Fig. 5 ODOE strategy for the case of three design parameters (X_1 , X_2 and X_3) with two levels.

2.2. Design of experiments (DOE)

The purpose of using the RSM is to construct an approximation relation between the true goal-function (response) and the training data. The accuracy of the RSM mostly depends on the quality of the training data selection. In order to minimize the size of training data, a reasonable strategy for training data selection needs to be applied. The theory of choosing suitable designs for exploring the entire design space efficiently is known as the DOE, which is employed to investigate the effective method for database establishment and synthetical analysis to reach the optimal project. There are many different DOE approaches. In this paper an ODOE is used. ODOE is an efficient method for analyzing multiple factors experiment, and can provide essential information with the smallest quantity of samples. After the number of design parameters is determined, the orthogonal array in which the factors (design parameters) are orthogonal to each other can be used to organize an experiment. Fig. 5 illustrates the ODOE strategy for the case of three design parameters (X_1 , X_2 and X_3) with two levels.

2.3. Flow solver

The numerical simulation was performed adopting the commercial CFD package of NUMECA. The code is based on a cell-centered finite-volume approach to solving the governing compressible Reynolds averaged Navier–Stokes (RANS)

equations, where the one-equation model of Spalart–Allmaras was used for turbulence modeling. A five-step Runge–Kutta algorithm was used for time marching. In order to speed up the convergence, local time stepping, residual smoothing and multigrid techniques were applied. The computational mesh was generated with grid generation tool of NUMECA/IGG software package. In order to meet the requirements of turbulence model, y^+ was controlled within 10.

To verify the accuracy of numerical simulation in the S-shaped duct with variable curvatures and adverse pressure gradients, the simulated duct performance was compared with the experiment conducted by Dueñas et al.² The duct geometry used by Dueñas et al.² is shown in Fig. 6, which was a 2D duct without struts. In Fig. 6, L is the duct length. The turbulence model used was Spalart–Allmaras model. The computational mesh was 541 (axial) by 57 (spanwise) nodes.

The two coefficients used to evaluate the performance of the duct in the paper are the static pressure coefficient and the total pressure loss coefficient. The static pressure coefficient is defined as

$$C_p = \frac{p - p_{\text{ref}}}{p^* - p_{\text{ref}}} \quad (1)$$

where p_{ref} denotes the static pressure at the reference location, p is the static pressure, p^* is the stagnation pressure, and the total pressure loss coefficient is defined as

$$\bar{\omega} = \frac{p_{\text{in}}^* - p_{\text{ex}}^*}{p_{\text{ref}}^* - p_{\text{ref}}} \quad (2)$$

where p_{in}^* , p_{ex}^* and p_{ref}^* are the stagnation pressure at inlet, exit and reference location, respectively.

Two figures comparing the experiments with the calculations are shown in Fig. 7. Fig. 7(a) shows the static pressure coefficient distribution on the duct inner and outer wall; and Fig. 7(b) demonstrates the duct exit spanwise profile of the total pressure loss coefficient. For the inner wall, Fig. 7(a) and (b) show a good agreement between the calculations and the measured static pressure coefficient and profiles of stagnation pressure loss coefficient at the exit. For the outer wall, Fig. 7(a) shows that the static pressure coefficient is accurately predicted by the Spalart–Allmaras turbulence model except in the region close to the peak, where the static pressure coefficient magnitude is underpredicted. Fig. 7(b) shows a significant difference between the inner wall and the outer wall. The order of the presence of the concave and convex wall curvatures in which the boundary layer experiences has a significant effect on the development of the boundary

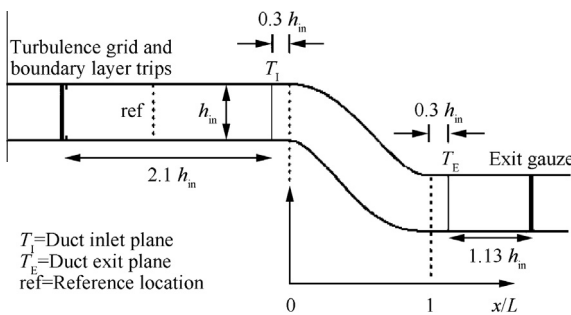


Fig. 6 Schematic of S-shaped duct rig.²

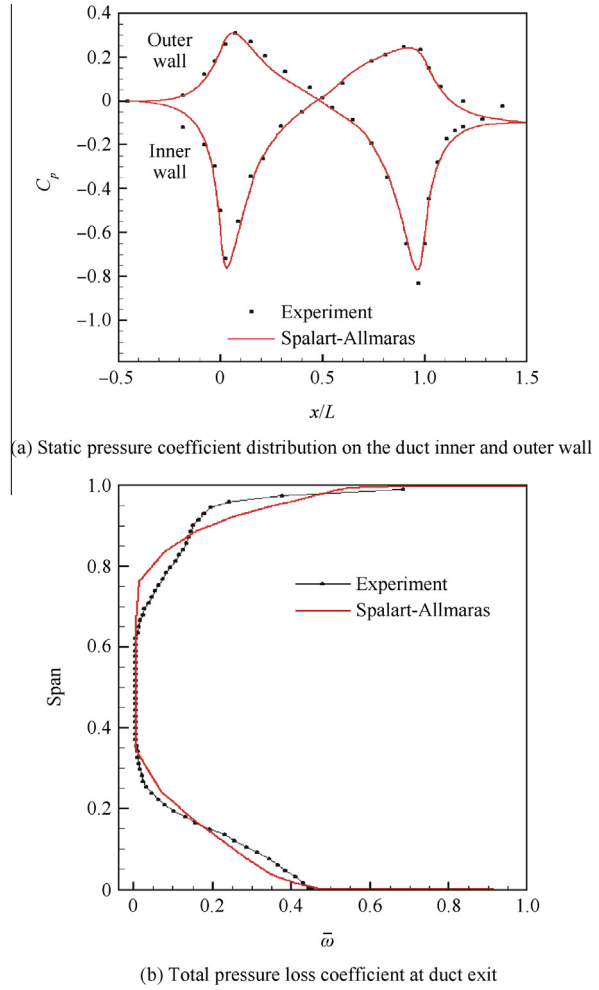


Fig. 7 Comparison of calculation with experiment.

layer on each wall. Between 65% and 85% height, the calculations under-predict the losses, while between 85% and 98% height, the calculations over-predict the losses, as shown in Fig. 7(b). Dueñas et al.², Britchford et al.²¹ pointed out that the development of boundary layer is affected by endwall curvatures. It is particularly difficult to model accurately the flow in the highly curved surface by Boussinesq eddy-viscosity turbulence models. Walker et al.³ discussed the challenge brought by the S-shaped duct to numerical methods in detail, and used an RSM and a standard wall function. Their study showed that Reynolds stress model is necessary in order to capture the effects of the streamline curvature in an aggressive S-shaped duct. Therefore, one potential cause for the discrepancy between the predicted and the measured spanwise profile of outer wall losses may be the lack of modeling of curvature effects in the Spalart–Allmaras turbulence model.

Although there is difference between the calculation and the experiment on the outer wall, the main flow features of the S-shaped duct could be captured by the numerical model used by this research. One reason we still insist on using the Spalart–Allmaras model is that according to previous simulation experience, a comparative discrepancy between each simulated configuration could still provide information to interpret the flow mechanism of endwall contouring. Another reason is that in

accurate prediction of separation, the absolute values of the total pressure loss, RANS CFD is quite unreliable. Hence, unless large eddy simulation (LES) or direct numerical simulation (DNS) is adopted, the Spalart–Allmaras model will be acceptable for this research.

2.4. Numerical optimization method

The optimization methods can be divided into local and global optimization algorithms. Although the local search algorithms based on gradient techniques are efficient in terms of convergence rates, they cannot guarantee discovery of the global optimum, and cannot be used when the design space is discontinuous. In contrast, the global search methods such as GAs offer the advantage of enhancing the probability of reaching the global optimum. Unfortunately, global search methods may require thousands of iterations to obtain the global optimum. It is very time consuming for the 3D numerical simulation of the flow field in turbomachinery. Therefore, in order to reduce the running time, the optimization approach presented here is to use an ANN to partially substitute the calculation of the flow field.

The optimization method used in this paper is summarized by Jin²² more detailedly, but the basic steps are:

- (1) Selecting the samples for the ANN.

The accuracy of the optimization depends on the neural network constructed by the database of design samples. The initial database is provided by an ODOE in this research to select the essential information with the smallest quantity of samples in the design space.

- (2) Training of the ANN.

After a sufficient initial database of samples has been generated, a training process is used to build a neural network. The network contains free parameters to fit database samples. A fitting process, also called learning process, is performed by back-propagation of the errors. The weight of each node is adjusted to minimize the overall error between the input and the output. After training, the network response surface model is defined.

- (3) Searching the global optimum of the RSM.

The searching process is performed by GA.

- (4) Verification of the optimal design.

The optimal endwall is evaluated by the 3D flow computation and added to the database. A comparison of the performance obtained by CFD with the one predicted by the neural network response surface model is performed. If there is not a good correlation, another iteration of design will start, repeating the same process until the optimum endwall is obtained. At the same time, the database grows after each iteration to provide more information of the design space, and therefore to better predict the real optimum.

3. Optimization test cases

Optimization cases of the axisymmetric and thenon-axisymmetric contouring in the S-shaped duct based on the endwall optimization system developed in this paper have been investigated. The aim of the optimization in the present work is to minimize the exit total pressure loss with the duct length

remaining constant. The total pressure loss coefficient has been defined by Eq. (2).

3.1. Datum duct

The duct with six struts is investigated in this paper. The meridional channel is shown in Fig. 8. The non-dimensional parameters of annular S-shaped duct are $\Delta R/L$, h_{in}/L , A_{ex}/A_{in} , r_{in}/h_{in} and t/c , where L , h and r are the duct length, height and radius, respectively; A is the duct area, while subscripts “in” and “ex” mean duct inlet and exit, respectively; t is the maximum thickness of strut; c is the strut chord. A summary of the main parameters is given in Table 1. The last column shows the typical values of the parameters of the ducts used in current engines according to Marios et al.²³ This classification would reveal that the investigated duct is to be fairly aggressive.

For the calculation of the duct, a long extension section parallel to the axial direction was used at the upstream and the downstream of the duct to allow for the development of the boundary layer and to minimize the interference between the duct static pressure field and the boundary conditions. Thus the CFD inlet plane is located $3h_{in}$ upstream of the duct inlet plane as shown in Fig. 8. The total number of the mesh grids is 444543. The datum duct along with the surface mesh used for the CFD analysis is shown in Fig. 9. The given inlet condition was total pressure, total temperature and angles of velocity. At the outlet boundary, radial equilibrium was applied with the static pressure being specified.

Fig. 10 shows the calculated pressure distribution around the strut at 5% and 50% span in the datum duct. There is a gradient change of pressure at the rear part of the strut in both lines. The change in the pressure gradient indicates that the strut has a hub corner separation.

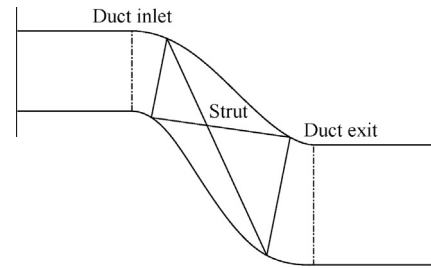


Fig. 8 Meridional channel of S-shaped duct.

Table 1 Main geometric parameters of annular S-shaped duct.

Parameter	Datum duct	Typical value of parameters
$\Delta R/L$	0.5	0.30–0.45
h_{in}/L	0.3	0.1–0.3
r_{in}/L	1.5	1.5–1.7
t/c	0.2	0.14–0.30
A_{ex}/A_{in}	1.0	0.6–0.7

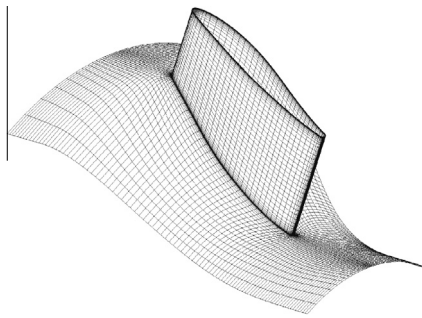


Fig. 9 Surface mesh of the datum duct.

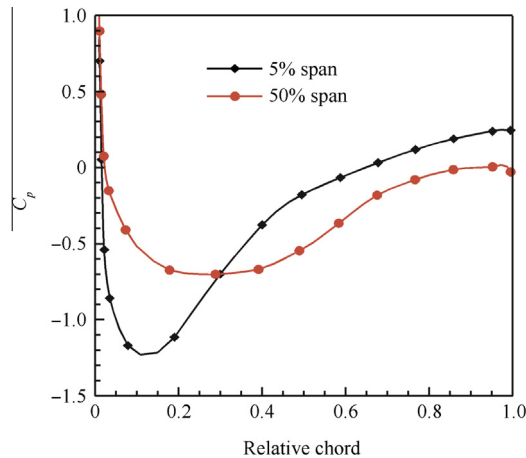


Fig. 10 Strut pressure distribution in the datum duct.

The computed near wall streamlines on the strut is shown in Fig. 11, from which the size and location of hub corner separation can be obtained. The separation occurs at approximately 45% chord after the maximum strut thickness (40% chord). Another significant phenomenon is the radial migration of the low momentum fluid because of the radial pressure gradient generated by wall curvatures. The low momentum fluid migrates up to 70% span. The separation results in a large-scale blockage in the duct and a rise in the total pressure loss coefficient. The calculation of the total pressure loss coefficient was 0.096. The loss coefficient distribution at the exit surface is shown in Fig. 12. The effect of the strut hub corner

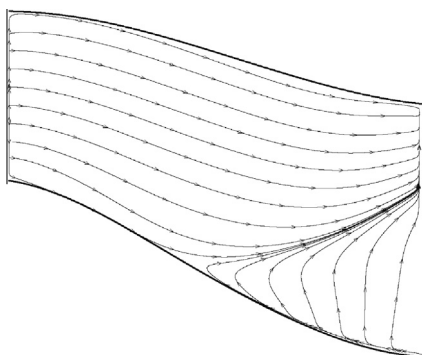


Fig. 11 Near wall streamlines on the strut in the datum duct.

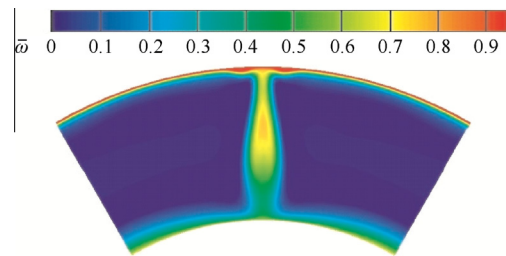


Fig. 12 Datum duct total pressure loss coefficient distribution at the exit surface.

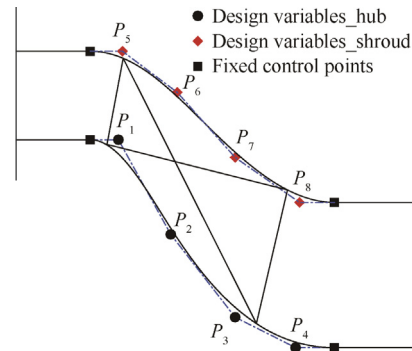


Fig. 13 Control points of axisymmetric endwall on meridional plane.

separation can be observed as the high loss region is between 50% and 80% span.

3.2. Optimization of axisymmetric contouring

The axisymmetric shape of the duct has been optimized for the minimum total pressure loss. The axisymmetric contouring endwall is generated by adjusting the flow passage of the meridional plane, and then rotates around the axis of the duct to produce the surface of the contoured endwalls. The optimization target is to minimize the duct total pressure loss defined by Eq. (3)

$$f = 1 - \bar{\omega} \quad (3)$$

The design optimization focuses on profiling both the hub and the casing endwalls. At each endwall, the profile of the perturbation is defined by a B-spline curve generated by six control points, giving four design variables and leaving two fixed control points at each end of the curve to maintain the endwall continuity. Therefore, there are eight design variables ($P_1 - P_8$) for the optimization of axisymmetric contouring, as shown in Fig. 13.

The scale of the design spaces has significant effect on the quality of the optimization problems, especially on the prediction accuracy of RSM. The investigation of Wallin and Eriksson¹⁵ shows that a large design space results in poor loss predictions for some of the extreme duct geometries evaluated. If the scale of the design space is too small, it cannot be guaranteed that the final result is the global optimum. In order to define a reasonable design space, DOE as mentioned earlier

was applied to analyze the influence of each design variable on the target function in the present research. The numerical simulation was carried out by the orthogonal experimental method, and the analysis was made on the design variables by using visual analysis method. The orthogonal table used here is $L_{27}(3^{13})$, which means that the experiments are conducted 27 times, containing 13 factors and each factor with three levels. It is not in the scope of this paper to investigate the procedure of the visual analysis method based on the ODOE, and more detailed description is given by Yang.²⁴

Fig. 14 shows the tendency of the influence of each design variable on the total pressure loss coefficient. Design variables were marked in Fig. 13. In Fig. 14 the x-axis represents the level of the design variables and the y-axis represents the statistic average value of the sum of different levels corresponding to the response for every design variables. That is to say, each point corresponding to the value of the y-axis on Fig. 14 is a statistic value. The range was used in the research to analyze the influence of each design variable on the response. The range, R , is defined as

$$R = \bar{K}_{\max} - \bar{K}_{\min} \quad (4)$$

where \bar{K}_{\max} and \bar{K}_{\min} are the maximum and the minimum of the average of the sum of different levels corresponding to the responses for the design variable respectively. Larger range of the design variable indicates that its impact on the response is greater than the others. Therefore, design variables P_6 and P_7 , as shown in Fig. 14, have a greater impact on the total pressure loss than the other design variables. Another noticeable phenomenon is that when design variable P_6 or P_7 is at a high level, the duct has a low total pressure loss. Therefore, the variation range of P_6 and P_7 are focused on the high level to reduce the exploration space. The analysis is the same for other design variables.

The calculated near wall streamlines on the strut in the axisymmetric optimal duct design is shown in Fig. 15. The separation region is significantly reduced compared with the datum duct. The boundary layer separates from the strut in the datum design at approximately 45% chord and extends to 70% of the duct span at the trailing edge. While the axisymmetric optimal strut-hub corner separation occurs at approximately 60% chord and extends to 30% of the duct height at

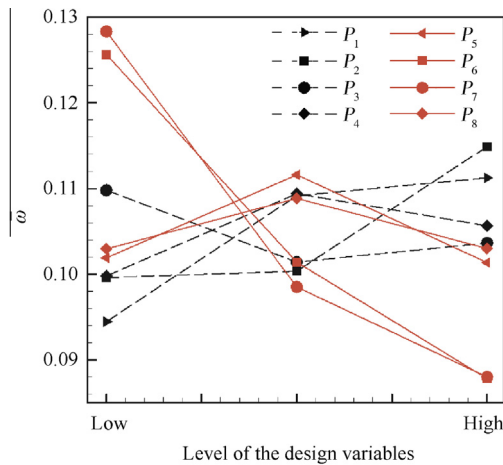


Fig. 14 Tendency of the influence of each design variable on the total pressure loss coefficient.

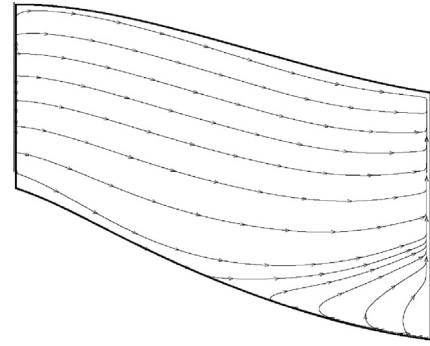


Fig. 15 Near wall streamline on the strut in the axisymmetric optimal duct.

the trailing edge. The optimal duct suppresses the corner separation to a large degree. The computed distributions of the total pressure loss coefficient at the exit of the axisymmetric optimized duct are shown in Fig. 16. The loss core associated with a large corner separation close to the shroud endwall in the datum duct (see Fig. 12) is due to the blockage of the larger separation close to the hub endwall. While the loss core in the axisymmetric optimal duct occurs close to the hub endwall because the separation region is reduced, (and the migration of the low momentum fluid is also suppressed). The optimal duct has a beneficial effect on the corner separation. The computed net duct loss is decreased by 27.7%.

The optimal design also indicates some important flow mechanisms for decreasing losses. The axisymmetric optimal duct design is compared with the datum duct in Fig. 17. The

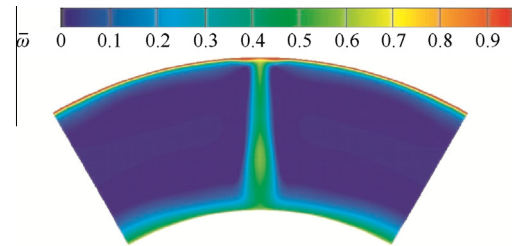


Fig. 16 Optimal axisymmetric duct total pressure loss coefficient distribution at the exit surface.

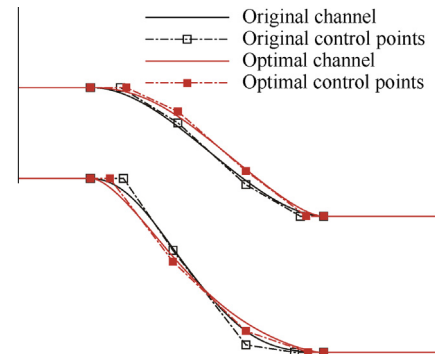


Fig. 17 Comparison of the datum and the axisymmetric optimal ducts.

most significant difference between the optimal and the datum ducts is the large increase of streamwise area distribution of the duct. This cross-section area of the duct flow passage, A_x , is defined as

$$A_x = \pi(R_{\text{shroud}_x}^2 - R_{\text{hub}_x}^2) \quad (5)$$

where R_{shroud_x} and R_{hub_x} are the shroud and the hub radius at different streamwise position x , respectively. This area was adjusted to compensate for the blockage caused by the strut. Another significant difference is the changed inner wall curvature. Increasing the convex curvature on the inner wall at the inlet of the duct can accelerate the flow earlier, and decreasing the concave curvature at the outlet of the inner wall can slow down the flow diffusion. Thus a lower streamwise pressure gradient is obtained to suppress the separation. Fig. 18 shows the area distribution of the datum and the optimal ducts. The area in the middle section of the duct is significantly enlarged to compensate for the blockage of the strut. The largest area occurs where the maximum thickness of the strut is. An early increased area from the duct inlet reduces the maximum velocity on the strut surface close to the inner wall, and then in the middle part of the duct area decreased which has the effect to accelerate the flow where the separation may occur. According to the visual analysis method presented above, the design parameters P_6 and P_7 (see Fig. 13) have a greater impact on the total pressure loss. From Fig. 17, it can be seen that the change of P_6 and P_7 has a direct influence on the area distribution, and dominates the performance of the duct. This is entirely consistent with the analysis discussed above. The change of other design variables is shown in Fig. 17.

3.3. Optimization of non-axisymmetric contouring

The non-axisymmetric endwall contouring was based on the datum duct. The design methodology for the endwall contouring was presented above. The non-axisymmetric endwall contouring was defined by B-spline surface controlled by 30 points, containing 12 design variables and 18 fixed control points. The non-axisymmetric endwall contouring was applied to the hub (Non_hub, see Fig. 19(a)) and shroud wall

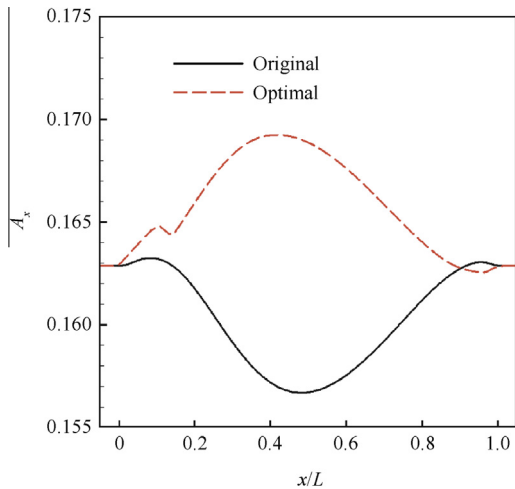


Fig. 18 Duct flow passage cross-section area distribution of the datum and optimal ducts.

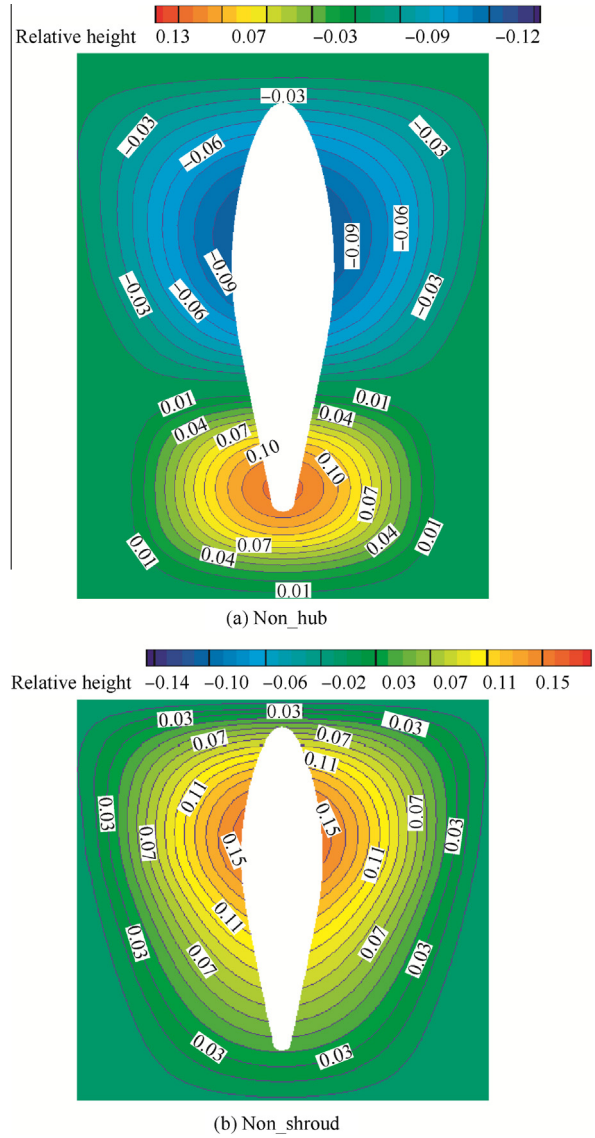


Fig. 19 Results of the optimal non-axisymmetric endwall contouring (viewed from the shroud to the hub).

(Non_shroud, see Fig. 19(b)) separately as well as to both the hub and the shroud wall (Non_both). In the datum duct, the static pressure field influenced by the strut was found to extend to approximately entire strut pitch. Therefore, the pitch of the endwall contouring was set at all strut pitches. The purpose of the contouring was to reduce the impact of the strut on the pressure field close to the hub. The optimization objective was to minimize the duct total pressure loss defined by Eq. (3), and the design space was also defined by ODOE described in the optimization of axisymmetric endwall contouring.

Fig. 20 shows the comparison of the exit total pressure loss coefficient of different endwall contouring applications. Compared with the datum, the exit total pressure loss coefficients of the Non_shroud, Non_hub, and Non_both have been decreased approximately by 23.0%, 29.6%, and 32.7%, respectively. The non-axisymmetric endwall contouring applied to both the hub and the shroud wall (Non_both, see Fig. 20,) has the lowest total pressure loss coefficient. Both

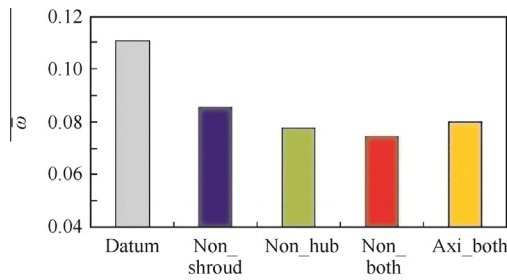


Fig. 20 Comparison of the exit total pressure loss coefficient for four endwall contouring applications.

Non_both and Non_hub have lower total pressure loss than the Axi_both (the axisymmetric endwall contouring applied to both the hub and the shroud wall). It can be also seen from Fig. 20 that the optimization results of the Non_hub and the Non_both are very close, indicating that the Non_hub has better optimization results than the Non_shroud. This is caused by the moderate change in the passage area after non-axisymmetric endwall contouring.

The results of the optimal non-axisymmetric endwall contouring applied to hub (Non_hub) and shroud (Non_shroud) wall separately is shown in Fig. 19(a) and Fig. 19(b), respectively, and the optimal non-axisymmetric endwall contouring results of Non_both is similar to that in Fig. 19. Blue contours are regions of reduced endwall height, and the red ones are regions of increased endwall height (compared with the datum duct). From the Non_hub endwall profile, it can be seen that there is a decrease in the endwall height of the front portion of the duct, and an increase in the endwall height of the rear portion. The presence of the contouring is to reduce the influence of the strut on the hub static pressure field. According to the principle of endwall contouring, convex wall curvature accelerates the flow and reduces the static pressure, while concave curvature causes diffusion and raises the static pressure. Therefore, at the area close to the strut leading edge, the profiling in the hub increases the convex curvature of the streamlines, lowering the static pressure to compensate for the raised static pressure caused by the front of the strut. At the area close to the maximum strut thickness, the contouring in the hub increases the concave curvature of the streamlines, so that the static pressure is raised to make up the reduced static pressure caused by the flow being accelerated by the strut, as shown in Fig. 19(a). At the trailing edge of the strut, the contouring in the hub increases the convex curvature of the streamlines, lowering the static pressure to compensate for the raised static pressure caused by the deceleration of the flow by the strut. At the area close to the exit of the duct, the contouring in the hub increases the concave curvature of the streamlines to raise the static pressure and raise the diffusion of the flow downstream of the strut.

The profiling of the shroud is straight forward, as shown in Fig. 19(b), which is concave curvature (viewed from the hub to the shroud) on the entire shroud wall, and reaches the maximum concave curvature near the maximum strut thickness. This kind of contouring will reduce the blockage caused by the strut geometry, but the drop of the exit total pressure loss coefficient is less than that of the contouring in the hub (Non_hub), as shown in Fig. 20, which is caused by the limitation in the circumferential boundary of the shroud wall.

That is to say, the shroud wall of the contoured endwall must be consistent with the datum shroud wall on the circumferential boundary, which was determined by the non-axisymmetric endwall parameterization method as shown in Fig. 3.

Fig. 21 shows a comparison of the pressure distribution at 5% span of the strut between the datum and the optimal ducts. The non-axisymmetric endwall contouring can be seen to reduce the peak velocity. At the same time, the position of the peak velocity significantly goes to the front part of the strut chord, indicating that there is less possibility that the optimal duct struts are going to experience corner separation than the datum duct struts, which can be seen from the surface streamlines of the optimal duct, as shown in Fig. 22.

Fig. 22 shows the near wall streamlines on the strut in the optimal non-axisymmetric duct. The effect of non-axisymmetric contouring is significant compared with that of the datum. The near wall surface streamlines for the optimal design do not show any reverse flow region on the strut surface. The corner separation appearing in the datum duct has been completely removed. Fig. 23 shows the exit total pressure loss coefficient distribution of the non-axisymmetric duct. The wake width of the optimal duct is significantly reduced compared with that of the datum duct. The endwall contouring can be seen to have reduced the high-loss region associated with the corner separation. In the hub region, it can be also

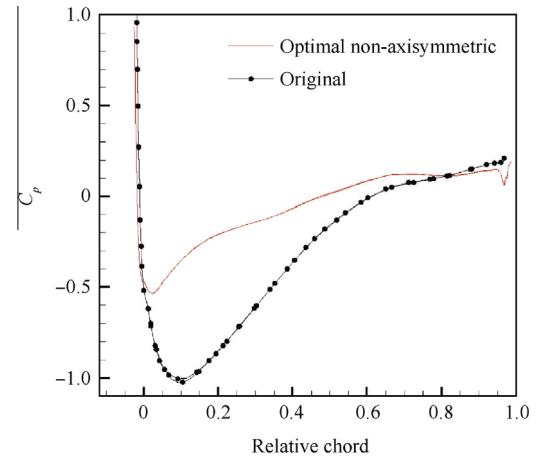


Fig. 21 Strut static pressure coefficient distribution in the datum and the optimal non-axisymmetric ducts (Non_both).

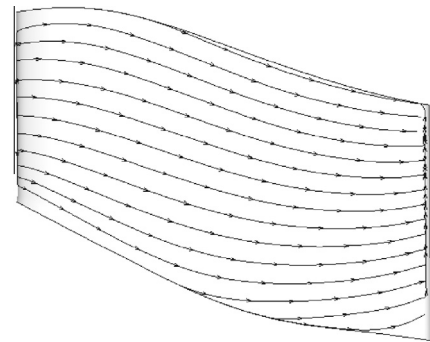


Fig. 22 Near wall streamlines on the strut in the optimal non-axisymmetric duct (Non_both).

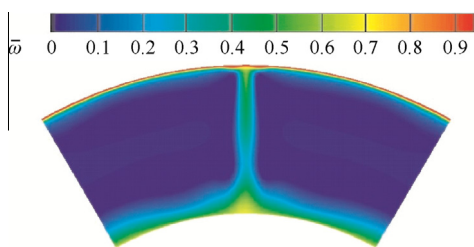


Fig. 23 Exit total pressure loss coefficient distribution of non-axisymmetric duct (Non_both).

seen that the loss over a region close to the hub wall at the downstream of the duct rose. The increase of the losses in this region results from the development of the corner boundary layer. The wake of the strut between 50% span and the casing is thinner than that in the datum duct, as the radial migration of the low momentum fluid is restricted by the endwall contouring.

4. Conclusions

- (1) The platform for endwall design optimization is constructed. It has been shown that the optimization method integrating AGA, DOE with RSM based on an ANN is a powerful tool, and can be used to obtain the optimal endwall shape which can lead to lower total pressure loss as well as good understanding of the flow mechanisms of endwall contouring.
- (2) Numerical optimization of the axisymmetric endwall contouring has been proved to be capable of suppressing corner separation and reducing the total pressure loss of a fairly aggressive duct significantly. One reason for these advantages is that enlargement of the passage area in the front part of the duct contributes to the decrease of the maximum velocity close to the inner wall, and reduction of the passage area in the middle part of the duct can accelerate the flow. The enlarged area effectively compensates for the blockage caused by the struts. Another reason is that increasing the convex curvature on the inner wall at the beginning of the duct and decreasing the concave curvature at the outlet of the inner wall will cause the flow to accelerate at the place where separation is most likely to occur. By means of adjusting the inner wall shape, a lowering of the stream-wise pressure gradient is obtained, contributing to the suppressing of the separation.
- (3) The optimal axisymmetric duct shows that the migration of the loss cores occupies 30% span from the hub at the exit of the duct because of the changed static pressure distribution, and the loss in the total pressure is decreased by 27.7% compared with that of the datum duct.
- (4) The non-axisymmetric endwall contouring was applied to reduce the total pressure loss of the duct. It was found that corner separation can be completely removed by adopting the optimal non-axisymmetric endwall, and the curvature of the hub endwall can have a significant influence on the total pressure loss and can be modified to minimize the disadvantageous pressure field caused by the strut. The non-axisymmetric contouring

performed on both the hub and the shroud endwall can be shown to reduce the total pressure loss by 32.7%, indicating that the non-axisymmetric endwall contouring has the potential to suppress the separation and to reduce the loss in the fairly aggressive duct.

Acknowledgements

The authors would like to thank the anonymous reviewers for their valuable comments on the manuscript. This work was supported by the National Natural Science Foundation of China (Nos. 51006005, 51236001), the National Basic Research Program of China (No. 2012CB720201), and the Fundamental Research Funds for the Central Universities of China.

References

1. Bailey DW, Britchford KM, Carrotte JF, Stevens SJ. Performance assessment of an annular S-shaped duct. *J Turbomach* 1997;**119**:149–56.
2. Dueñas CO, Miller RJ, Hodson HP, Longley JP. Effect of length on compressor inter-stage duct performance. *Proceedings of ASME Turbo Expo 2007: power for land, sea, and air*; 2007 May 14–17; Montreal, Canada. New York: ASME; 2007.
3. Walker AD, Barker AG, Carrotte JF, Bolger JJ, Green MJ. Integrated outlet guide vane design for an aggressive S-shaped compressor transition duct. *J Turbomach* 2013;**135**(1):011035.
4. Rose MG. Non-axisymmetric endwall profiling in the HP NGV's of an axial flow gas turbine. *Proceedings of international gas turbine and aeroengine congress and exposition*; 1994 Jun 13–18; The Hague, Netherlands. New York: ASME; 1994.
5. Hartland JC, Gregory-Smith DG, Rose MG. Non-axisymmetric endwall profiling in a turbine rotor blade. *Proceedings of international gas turbine and aeroengine congress and exposition*; 1998 Jun 2–5; Stockholm, Sweden. New York: ASME; 1998.
6. Harvey NW, Bernnan G, Newman DA, Rose MG. Improving turbine efficiency using non-axisymmetric end walls: validation in the multi-row environment and with low aspect ratio blading. *Proceedings of ASME Turbo Expo 2002: power for land, sea, and air*; 2002 June 3–6; Amsterdam, The Netherlands. New York: ASME; 2002.
7. Torre D, Vázquez R, de la Rosa Blanco E, Hodson HP. A new alternative for reduction of secondary flows in low pressure turbines. *Proceedings of ASME Turbo Expo 2006: power for land, sea, and air*; 2006 May 8–11; Barcelona, Spain. New York: ASME; 2006.
8. Sonoda T, Hasenjäger Martina, Arima T, Sendhoff B. Effect on endwall contouring on performance of ultra-low aspect ratio transonic turbine inlet guide vanes. *Proceedings of ASME Turbo Expo 2007: power for land, sea, and air*; 2007 May 14–17; Montreal, Canada. New York: ASME; 2007.
9. Mahmood G, Acharya S. Measured endwall flow and passage heat transfer in a linear blade passage with endwall and leading edge modifications. *Proceedings of ASME Turbo Expo 2007: power for land, sea, and air*; 2007 May 14–17; Montreal, Canada. New York: ASME; 2007.
10. Gustafson R, Mahmood G, Acharya S. Aerodynamic measurements in a linear turbine blade passage with three-dimensional endwall contouring. *Proceedings of ASME Turbo Expo 2007: power for land, sea, and air*; 2007 May 14–17; Montreal, Canada. New York: ASME; 2007.
11. Hoeger M, Cardamone P, Fottner L. Influence of endwall contouring on the transonic flow in a compressor blade. *Proceedings of ASME Turbo Expo 2002: power for land, sea, and*

- air; 2002 Jun 3–6; Amsterdam, The Netherlands. New York: ASME; 2002.
12. Harvey NW. Some effect of non-axisymmetric end wall profiling on axial flow compressor aerodynamics. Part I: Linear cascade investigation. *Proceedings of ASME Turbo Expo 2008: power for land, sea, and air*; 2008 Jun 9–13; Berlin, Germany. New York: ASME; 2008.
13. Harvey NW, Offord TP. Some effect of non-axisymmetric end wall profiling on axial flow compressor aerodynamics. Part II: Multi-stage HPC CFD study. *Proceedings of ASME Turbo Expo 2008: power for land, sea, and air*; 2008 Jun 9–13; Berlin, Germany. New York: ASME; 2008.
14. Wallin F, Eriksson L. Non-axisymmetric endwall shape optimization of an intermediate turbine duct. *Proceedings of 18th ISABE conference*; 2007.
15. Wallin F, Eriksson L. Response surface-based transition duct shape optimization. *Proceedings of ASME Turbo Expo 2006: power for land, sea, and air*; 2006 May 8–11; Barcelona, Spain. New York: ASME; 2006.
16. Naylor EMJ, Dueñas CO, Miller RJ, Hodson HP. Optimization of non-axisymmetric endwalls in compressor S-shaped ducts. *J Turbomach* 2010;**132**(1):011011.
17. Jin DH, Gui XM. Aerodynamic design optimization of cascade airfoils based on multiobjective genetic algorithm. *J Aerosp Power* 2007;**22**(2):285–90 [Chinese].
18. Jin DH, Gui XM. Numerical design optimization of compressor blade based on ADOP. *J Aerosp Power* 2007;**22**(11):1903–8 [Chinese].
19. Jin DH, Chen J. Multi-point aerodynamic design optimization for compressor cascade airfoils. *J Propul Technol* 2007;**28**(4):367–72 [Chinese].
20. Ning FF, Liu XJ. A new response surface model and its applications in the aerodynamic optimization of axial compressor blade profile. *Acta Aeronaut Astronaut Sin* 2007;**28**(4):813–20 [Chinese].
21. Britchford KM, Carrotte JF, Stevens SJ, McGuirk JJ. The Development of the mean flow and turbulence structure in an annular S-shaped duct. *Proceedings of international gas turbine and aeroengine congress and exposition*; 1994 Jun 13–18; The Hague, Netherlands. New York: ASME; 1994.
22. Jin DH. Numerical design optimization of axial compressor blades and airfoils dissertation. Beijing: Beihang University; 2007 [Chinese].
23. Marios KK, Naylor EMJ, Miller RJ, Hodson HP. The effect of an upstream compressor on a non-axisymmetric S-duct. *Proceedings of ASME Turbo Expo 2010: power for land, sea, and air*; 2010 Jun 14–18; Glasgow, UK. New York: ASME; 2010.
24. Yang D. *Design and analysis of experiments*. Beijing: China Agriculture Press; 2002 [Chinese].

Jin Donghai is an associate professor at the School of Energy and Power Engineering, Beihang University. He received the Ph.D. degree from the same university in 2007. His main research interests are secondary flow control mechanism and aerodynamic numerical optimization design method.

Liu Xiwu is a Ph.D. candidate at Beihang University. His main research interest is endwall flow control technology.